agriculture

MDPI

Article

Compressive Characteristics and Fracture Simulation of Cerasus Humilis Fruit

Cheng Hao [1,2], Dongjin Yang [1,2], Liyang Zhao [1,2], Jianguo Yang [1,2], Tao Wang [1,2] and Junlin He [1,2,*]

[1] College of Agricultural Engineering, Shanxi Agricultural University, Jinzhong 030801, China; 20231001@stu.sxau.edu.cn (C.H.); 20233049@stu.sxau.edu.cn (D.Y.); 20233050@stu.sxau.edu.cn (L.Z.); 20233753@stu.sxau.edu.cn (J.Y.); z20223015@stu.sxau.edu.cn (T.W.)

[2] Shanxi Provincial Key Laboratory of Key Technology and Equipment for Dryland Agricultural Machinery, Jinzhong 030801, China

* Correspondence: hejunlin@sxau.edu.cn

Abstract: During the harvesting process of Cerasus humilis, the fruits are susceptible to compression and impacts from the combing teeth, leading to internal damage to the pulp and rupture of the peel. This compromises the quality of the harvested fruits and subsequent processing, resulting in significant economic losses. To investigate the mechanical behavior of Cerasus humilis fruit, this study measured the geometric parameters as well as the mechanical properties (failure load, elastic modulus, compressive strength, and fracture energy) of the peel, pulp, and core in both the axial and radial directions. A geometric model of Cerasus humilis fruit was constructed using three-dimensional reverse engineering technology. The rupture process of the fruit under compressive loading was simulated and analyzed using Abaqus software (Version 2023). The damage mechanisms were investigated, and the accuracy and reliability of the finite element model were validated through compression experiments. The experimental results indicated that the mechanical properties of the peel of Cerasus humilis fruit exhibited no significant differences between the axial and radial directions, allowing it to be regarded as an isotropic material. In contrast, the mechanical properties of the pulp and core showed significant differences in both directions, demonstrating anisotropic characteristics. Additionally, the axial compressive strength of the Cerasus humilis fruit was higher than its radial compressive strength. The simulation results revealed that during axial compression, when the surface stress of the peel reached 0.08 MPa, the fruit completely fractured. The location and morphology of the cracks in the simulation were consistent with those observed in the experimental results. Furthermore, under different compression directions, the force–displacement curves obtained from actual compression tests closely aligned with those from the finite element simulations. The finite element model established in this study effectively simulates and predicts the cracking and internal damage behavior of Cerasus humilis fruit under compressive loads. This research provides a theoretical foundation and technical guidance for reducing mechanical damage during the harvesting process of Cerasus humilis.

Keywords: Cerasus humilis fruit; mechanical properties; compression; damage; finite element simulation

Academic Editor: Maohua Xiao

Received: 31 October 2024
Revised: 26 December 2024
Accepted: 29 December 2024
Published: 2 January 2025

Citation: Hao, C.; Yang, D.; Zhao, L.; Yang, J.; Wang, T.; He, J. Compressive Characteristics and Fracture Simulation of Cerasus Humilis Fruit. *Agriculture* **2025**, *15*, 88. https://doi.org//10.3390agriculture15010088

1. Introduction

Cerasus humilis, native to China, is mainly distributed in the provinces and regions of Shanxi, Hebei, Liaoning, Inner Mongolia, and others [1]. Along with Russian large-fruited sea buckthorn, goji berry, and American blueberry, Cerasus humilis is collectively known as

one of the world's four rare health-promoting fruits. Its fruit is rich in nutrients, including 17 amino acids required by the human body, and abundant amounts of vitamin C, vitamin B_2, vitamin E, as well as minerals such as potassium, phosphorus, zinc, and selenium. Notably, its calcium content is the highest among fruits, earning it the nickname "calcium fruit" [2,3]. The primary harvesting method for Cerasus humilis is mechanical combing harvesting [4–6]; the high-speed rotating comb teeth exert compression and impact on the fruit [7], leading to internal pulp damage and peel rupture. This affects the quality of the harvested fruit and subsequent processing. Therefore, comprehensively understanding the biomechanical properties of the fruit, constructing a highly reliable mechanical model, thoroughly studying its compressive damage, and analyzing its damage mechanisms have important fundamental research value and industrial significance.

Currently, considerable theoretical and practical foundations have been established regarding the mechanical properties of fruits. Yang Yuxiao et al. [8] investigated the mechanical property parameters of Korla fragrant pears at different maturity stages. They established mathematical models describing the relationship between the static compression damage area and deformation amount for pears at various maturity levels, and predicted the damage resulting from static compression during different harvesting periods. Through puncture tests, Tong Bin et al. [9] studied the mechanical properties of three Cerasus humilis varieties at different temperatures. The experimental results demonstrated that temperature has a significant effect on the puncture failure stress of different Cerasus humilis varieties. As the temperature increased, the puncture failure stress of Cerasus humilis decreased; thus, low-temperature environments help reduce mechanical damage. Xue Zhong et al. [10] determined the mechanical property parameters of various tissues in pineapple through tensile and compressive tests and shear strength tests. Ihueze Christopher Chukwutoo et al. [11] measured the mechanical properties of citrus fruits through compression tests. The experimental results showed that the radial compressive ultimate stress and maximum contact stress of citrus are greater than those under axial compression. Based on the distortion energy theory (DET) and the maximum shear stress theory (MSST), the yield strengths of citrus during storage and transportation were determined to be 0.03 MPa and 0.01 MPa, respectively.

With the continuous development of finite element theory, numerical simulation techniques have become an effective approach for studying the mechanical properties of agricultural products under real-world loads, enabling efficient analysis and prediction of their damage behavior [12]. Kang Shilei et al. [13] combined physical experiments and numerical simulations to calibrate the mechanical parameters of Cerasus humilis fruit. Ihueze Christopher Chukwutoo et al. [14] combined Hertz contact stress theory with the finite element method to study the maximum contact stress and ultimate stress of citrus fruits under transportation and storage conditions. They simulated and determined the characteristics of the elastic limit stress, elastic modulus, Poisson's ratio, and bio-yield stress of citrus fruits in both the axial and radial directions. Caglayan Nuri et al. [15] conducted compression tests on potatoes and utilized a method combining reverse engineering, high-speed imaging, and finite element analysis to examine the deformation of potato tuber samples when dropped from different heights. They predicted the stress distribution and the degree of damage after impact. Ben Zongyou et al. [16] determined the mechanical properties (elastic modulus, compressive strength, and fracture energy) of gluten in both the axial and radial directions under different moisture contents and aspect ratios. Utilizing Abaqus software, they developed a finite element model with cohesive elements to simulate the compression fracture process of gluten pellets. The simulation results closely matched the experimental data, with a relative error of 4–7%. In summary, most researchers have

only studied the stress distribution during compression, and there are few reports on the fracture process of fruits under compressive loads.

In this study, a combined method of numerical simulation and experimentation was employed to investigate the mechanical properties and compression damage mechanisms of Cerasus humilis fruit. First, mechanical tests were conducted to determine the mechanical parameters of each tissue of the fruit, namely the peel, pulp, and core. Then, three-dimensional reverse engineering technology was used to accurately construct 3D geometric models of the peel, pulp, and core. Finally, the compression cracking process of Cerasus humilis fruit was simulated using the Abaqus finite element analysis software to obtain the stress distribution and cracking conditions under compressive loads. The compression damage mechanisms were analyzed, and the simulation results were compared with the experimental data to verify the accuracy and stability of the finite element model. This research provides theoretical guidance for reducing compression damage during the harvesting of Cerasus humilis and for optimizing the design of harvesting equipment.

2. Materials and Methods

2.1. Materials and Equipment

In this study, fresh and mature "Nongda No. 6" Cerasus humilis fruits were selected as the research materials. They were harvested from the Cerasus humilis experimental field at Shanxi Agricultural University (longitude: 112°36′56″ E; latitude: 37°25′17″ N). All fruits were hand-picked to ensure consistent ripeness and no damage. The harvested fruits were stored in a constant-temperature incubator at 25 °C with a relative humidity of 80% for later use, with the storage time not exceeding 24 h. Mechanical property tests were conducted using a universal testing machine (INSTRON-5544, Instron Corporation, Norwood, MA, USA) equipped with a 2 kN load cell, with a measurement error of ±0.5%. Other instruments required for the experiment included a digital vernier caliper (Wenling Kaichuang Measuring Tools Co., Ltd., Taizhou, China, accuracy ± 0.01 mm), an electronic balance (Hangzhou Hengyi Instrument Technology Co., Ltd., Hangzhou, China. accuracy ±0.01 g), a drying oven (DHG-9023A, Wuxi Sanxin Precision Testing Equipment Co., Ltd., Wuxi, China), utility knives, and pulp samplers (Beijing Nanbei Chenyang Experimental Equipment Co., Ltd., Beijing, China). Prior to the experiment, 100 fruits with similar shapes and uniform masses, and without visible damage were randomly selected, labeled, and left at room temperature for two hours. The basic dimensions of the fruits—length (L), width (W), and height (H)—were measured using a vernier caliper, as shown in Figure 1a. The fruit's internal structure upon axial sectioning is shown in Figure 1b.

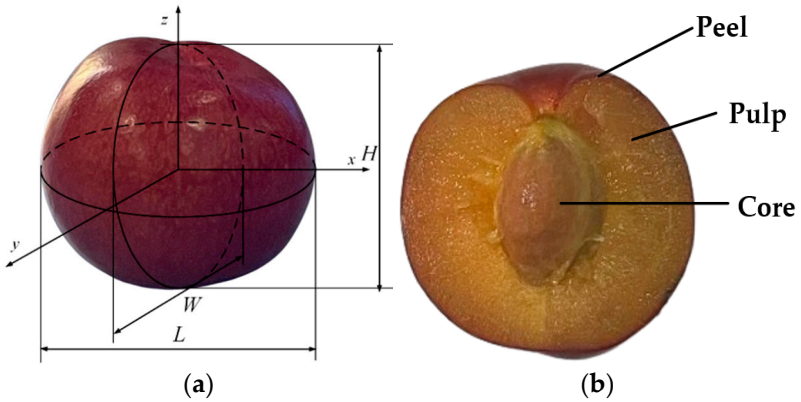

Figure 1. Cerasus humilis. (**a**) Three-axis dimensions of Cerasus humilis fruit; (**b**) cross-section of cerasus humilis fruit.

2.2. Determination of Moisture Content in Cerasus Humilis Fruit

Ten Cerasus humilis fruits were randomly selected. The moisture content of the fruit was determined by direct drying method [17] Standard (GB 5009.3-2016). The average value of the calculated results was taken, and the calculation formula is as follows:

$$X = \frac{m_1 - m_2}{m_1 - m_3} \times 100\% \quad (1)$$

where X represents the moisture content of the Cerasus humilis fruit (%); m_1 is the mass of the empty aluminum container and the sample (g); m_2 is the mass of the empty aluminum container and the dried sample (g); and m_3 is the mass of the empty aluminum container (g).

2.3. Mechanical Property Tests of Various Tissues of Cerasus Humilis

The peel, as the outermost tissue of Cerasus humilis fruit, plays a critical protective role in reducing mechanical damage [18]. To analyze the differences in the axial and radial mechanical properties of the Cerasus humilis peel, a utility knife was used to cut the peel along the axial direction into rectangular specimens measuring 40 ± 0.5 mm in length and 10 ± 0.5 mm in width. Any excess pulp adhering to the back of the peel was carefully scraped off, resulting in a thickness of 0.3 ± 0.1 mm. Before the test, to prevent the fruit peel from slipping, the peel samples were fixed in a fixture with a rubber pad and stretched at a loading rate of 5 mm/min [19]. The test was stopped upon peel rupture, and specimens that fractured near the middle region were selected as valid tensile samples. Using a sampler, the pulp was made into cylindrical specimens along the axial direction of the Cerasus humilis fruit; each sample had a height of 15 ± 0.5 mm and a diameter of 8 ± 0.5 mm. The compression test was conducted using a platen compression method. During the experiment, both types of samples were placed in the support fixture and centered on the compression plates. The distance between the grips and the sample was finely adjusted using the displacement control button. Once the platen made slight contact with the sample surface, the compression force and displacement were reset. The universal testing machine was set to a loading speed of 5 mm/min. The loading process was initiated by pressing the start button and stopped when the sample experienced compressive failure. The preparation and testing procedures for the radial samples were identical to those for the axial samples. The ellipsoidal core of Cerasus humilis fruits is embedded within the pulp, offering support and minimizing fruit deformation. During the experiment, the excess flesh surrounding the core was scraped off, and the core sample was placed in the support fixture, centered on the compression plates. Loading was applied along both the short and long axes of the core at a rate of 5 mm/min until the core fractured. The corresponding force–displacement curves and test data were recorded using a universal testing machine. Each test was repeated five times, and the average value was taken as the test result. The mechanical property testing process is shown in Figure 2. After completing the experiment, the data were processed using Origin 2024b (Origin Lab, Northampton, MA, USA). The mechanical property parameters of each tissue of Cerasus humilis fruits were calculated according to Formulas (2)–(6) [20]:

$$\sigma = \frac{F}{S} \quad (2)$$

$$\varepsilon = \frac{\Delta L}{L} \quad (3)$$

$$E = \frac{\sigma}{\varepsilon} = \frac{FL}{S\Delta L} \quad (4)$$

$$E_p = \int_0^l f(x)dx \tag{5}$$

$$G = \frac{E}{2(1+\mu)} \tag{6}$$

where σ is the stress (MPa); F is the tensile force (N); S is the cross-sectional area of the material in the tensile (compression) direction (mm^2); ε is the tensile (compression) strain (%); ΔL is the length after deformation (mm); L is the original length before deformation (mm); E is the elastic modulus of the material (MPa); E_p is the fracture energy of the material (mJ); $f(x)$ is the force–displacement curve of the material under tension or compression; and l is the displacement corresponding to the first peak point on the curve (mm).

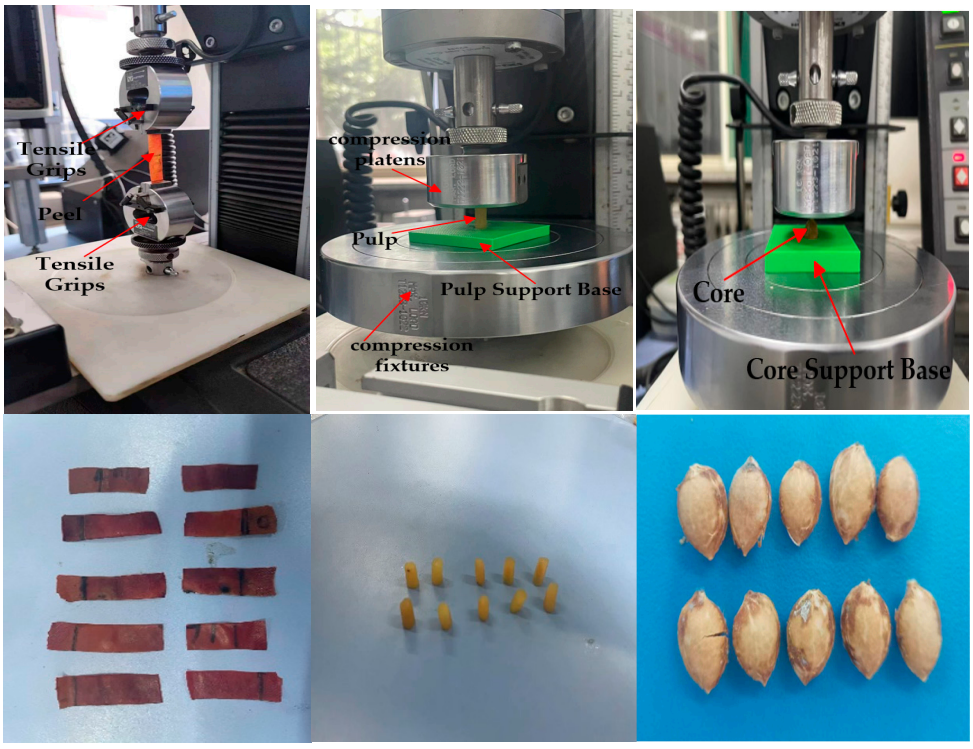

Figure 2. Mechanical property tests of different tissues of cerasus humilis fruit. (**a**) Peel tensile test; (**b**) pulp compression test; (**c**) core compression test.

2.4. Compression Test of Cerasus Humilis Fruit

In order to understand the fracture process of Cerasus humilis fruit under compressive loads and to verify the accuracy of simulation results, we selected 10 Cerasus humilis fruits of similar size and without damage, removed their stalks to minimize interference with the mechanical tests [21], and conducted compression tests along the axial and radial directions. During the test, the loading rate of the universal testing machine was set to 5 mm/min, and loading was stopped after the fruit cracked. The force-displacement data obtained from the experiment were automatically recorded by the computer, and the experimental procedure is shown in Figure 3.

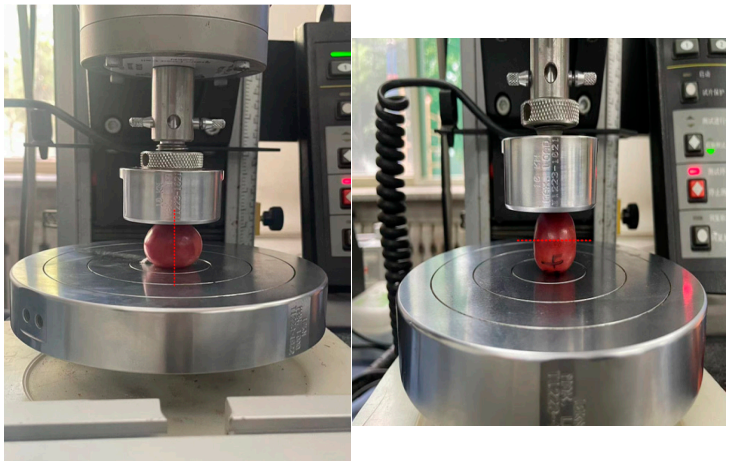

(**a**) (**b**)

Figure 3. Compression tests of Cerasus humilis fruit. (**a**) Axial compression test; (**b**) radial compression test.

2.5. Finite Element Modeling and Simulation

2.5.1. Geometric Model Construction

To enhance the feasibility of the study and reduce the complexity of the model, it was assumed that there is complete adhesion between the core and the pulp, without separation [22]. During modeling, the core was embedded as an independent geometric entity within the flesh structure. Geometric entity modeling is key to improving simulation accuracy. Given the irregular shape of Cerasus humilis fruit, one fruit was randomly selected from the test samples. A handheld 3D scanner (HandySCAN 700, Creaform, Lévis, QC, Canada; scanning accuracy of 0.03 mm, scanning measurement rate of 480,000 measurements/second, scanning resolution of 0.05 mm) was used to collect point cloud data of its surface and core. The open-source software CloudCompare v2.13.2 (EDF R&D, Chatou, France) was utilized to reconstruct the point cloud data, generating an initial mesh model. Subsequently, the mesh model was imported into SolidWorks (Dassault Systèmes s.a, Waltham, MA, USA) for further processing. Surface editing tools were used to refine the surface details, completing the geometric modeling of the peel, flesh, and core. Finally, in SolidWorks, the peel, pulp, and core were assembled, and constraints were applied to ensure that the positional relationships between the geometric entities were consistent with the actual structure of Cerasus humilis fruit, thus forming a complete geometric model of the fruit. The modeling process of Cerasus humilis fruit is shown in Figure 4.

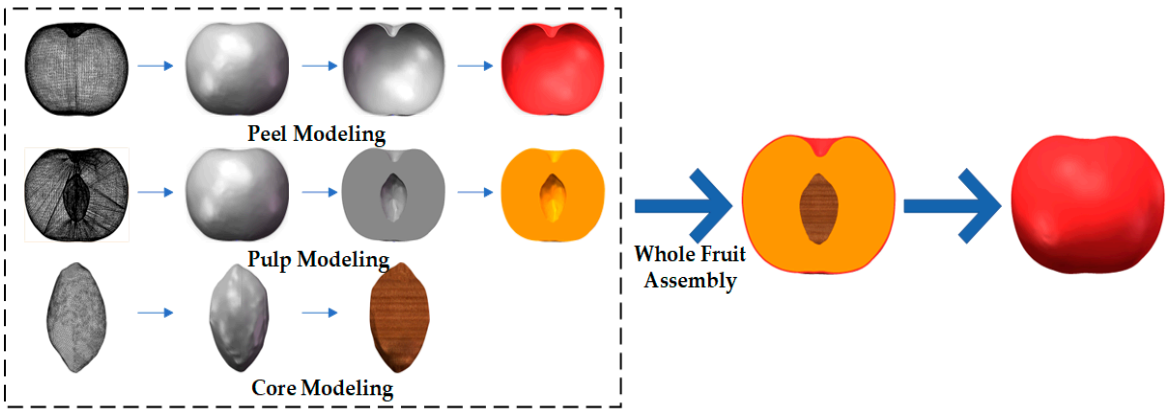

Figure 4. Establishment of the geometric model of Cerasus humilis fruit.

2.5.2. Finite Element Modeling and Meshing

In this research, finite element simulations were conducted using Abaqus (Version 2023, Dassault Systèmes, Paris, France). In finite element analysis, the mesh type and mesh size have a significant impact on the accuracy of the simulation. Common mesh types include tetrahedral meshes and hexahedral meshes. Tetrahedral elements, due to their flexible shapes, can better adapt to complex and irregular geometries; however, at the same mesh density, the simulation accuracy is usually lower. In contrast, hexahedral elements, owing to their regular shapes and higher-order shape functions, can provide a higher accuracy and better numerical stability at the same mesh density [23]. Moreover, smaller mesh sizes help to capture subtle variations in the physical fields more accurately. Based on the above considerations and to adapt to the size of the Cerasus humilis fruit and meet the computational speed and solution accuracy requirements, this study employed hexahedral meshes with a global mesh size of 0.5 mm [24,25]. The Cerasus humilis model was imported into the Hypermesh software in Altair HyperWorks 2020 (Altair Engineering, Inc., Troy, MI, USA) for mesh preprocessing. The peel, pulp, and core of Cerasus humilis fruit were meshed separately to ensure that the mesh quality met the analysis requirements. The numbers of elements and nodes for each tissue of Cerasus humilis after meshing are shown in Table 1. The mesh details and compression directions are shown in Figure 5.

Table 1. Number of mesh elements and mesh types for each tissue of Cerasus humilis fruit.

Material	Number of Nodes	Number of Grids	Mesh Type
Peel	22,117	11,051	C3D8
Pulp	8707	7746	C3D8R
Core	13,702	12,189	C3D8R

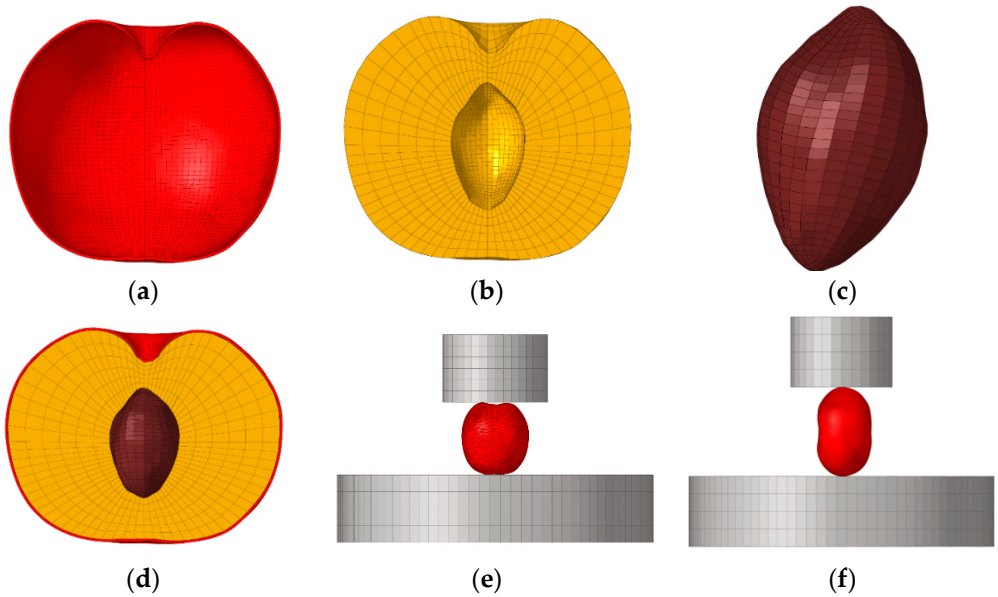

Figure 5. Finite element simulation modeling. (**a**) Peel; (**b**) pulp; (**c**) core; (**d**) cross-section of Cerasus humilis fruit; (**e**) axial compression finite element model; (**f**) radial compression finite element model.

2.5.3. Ductile Damage Model

In Abaqus, the Ductile Damage model was used to simulate the damage and failure behaviors of materials due to the formation, growth, and coalescence of voids within the material during plastic deformation [26,27]. The processes of damage initiation and damage evolution are shown in Figure 6. This model is widely applied to predict phenomena such as damage accumulation and the ultimate failure of materials under tensile and compressive

loads. By incorporating this model, material damage mechanisms can be introduced into finite element analyses, enabling a more accurate simulation of the material failure process.

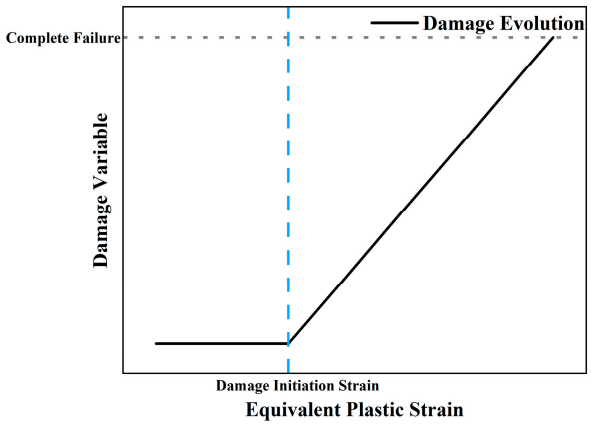

Figure 6. Ductile Damage model: damage initiation and evolution.

This study adopted a damage initiation criterion based on equivalent plastic strain. When the equivalent plastic strain of the material (ε_p^{eq}) reaches a predetermined critical value (i.e., fracture strain, ε_p^f), the damage initiation criterion is triggered, and the model begins to compute the material's damage. The fracture strain represents the maximum equivalent plastic strain the material can withstand and can be determined from mechanical test data. Its calculation formula is shown in Equation (7) and it was used to identify the onset of material damage.

$$\varepsilon_p^f = \varepsilon_{\text{total}} - \frac{\sigma_f}{E} \tag{7}$$

where ε_p^f is the fracture strain; $\varepsilon_{\text{total}}$ is the total strain; E is the elastic modulus; and σ_f is the fracture stress.

Before damage occurs, the material follows an elastoplastic constitutive relationship, with the equivalent plastic strain gradually accumulating. This constitutive relationship is described in Equation (8). When $\varepsilon_p^{eq} \geq \varepsilon_p^f$, the material enters the damage evolution phase, during which a damage variable D is introduced to describe the degradation of material stiffness. The constitutive relationship for the material in the damage evolution phase is expressed in Equation (9). As D increases, the effective stiffness of the material gradually decreases. When D = 1, the material completely fails and loses its load-bearing capacity. Through the relationship between equivalent plastic strain and fracture strain, the model effectively captures the entire process from elastoplastic behavior to damage evolution and ultimate failure.

$$\boldsymbol{\sigma} = \boldsymbol{D}^e : \boldsymbol{\varepsilon}^e \tag{8}$$

$$\boldsymbol{\sigma} = (1 - D)\boldsymbol{D}^e : \boldsymbol{\varepsilon}^e \tag{9}$$

where σ is the stress tensor; $\boldsymbol{D}^e$ is the material's elastic stiffness matrix; $\boldsymbol{\varepsilon}^e$ is the strain tensor; and D is the damage variable and $0 \leq D \leq 1$.

2.5.4. Boundary Conditions and Solutions

The mesh model established in Hypermesh was imported into ABAQUS. Based on the results of the mechanical tests, the peel and pulp were defined as elastoplastic materials [28]. During the compression process of Cerasus humilis fruit, the core does not undergo damage; therefore, it was simplified as a linear elastic material. The Ductile Damage model was used to define the damage behavior of the peel and pulp, with the damage evolution type set to displacement and a parameter value of 1×10^{-8}. The remaining material properties

and damage parameters are presented in Table 2. Using the TIE tool, the inner surface of the peel, the outer surface of the pulp, the inner surface of the pulp, and the outer surface of the core were tied together into a single entity. The base and the indenter were set as rigid bodies. A fixed constraint was applied to the base, a displacement constraint was applied in the negative Y-direction to the indenter, and its degrees of freedom were constrained in the other directions. The compression displacement was 10 mm. General contact was used for the contact interactions, with the friction coefficient between the Cerasus humilis fruit and the indenter and support set to 0.01 [29]. The ABAQUS/Implicit solver was utilized for computation. The maximum number of increments was set to 20,000, the initial increment size to 0.01, and the minimum increment size to 1×10^{-6}.

Table 2. Material simulation parameters.

Material	E (MPa) [1]		Plasticity Parameters		μ [2] [30]	ρ [3] (g/cm^3)	Ductile Damage Model		
	E_1	E_2	Yield Stress	Plastic Strain			Fracture Strain	Stress Triaxiality	Strain Rate
Peel	1.40	1.40	1×10^{-6}	0	0.3	1.05	0.01	1	1
Pulp	0.23	0.58	0.03 0.04	0 0.2	0.4	1.05	0.2	1	1
Core	73.11	60.18	-	-	0.3	1.15	-	-	-

[1] E: elastic modulus. E_1: axial elastic modulus E_2: radial elastic modulus. [2] μ: Poisson's ratio. [3] ρ: density.

3. Results and Discussion

3.1. Geometric Parameters and Mechanical Properties of Cerasus Humilis Fruit

According to the measurement results for the moisture content, the average moisture content of the "Nongda No. 6" fruits was 84.72 ± 0.03%. Using a vernier caliper, the mean and standard deviation of the length of the Cerasus humilis fruits were measured to be 26.13 ± 1.59 mm, the width was 27.11 ± 1.73 mm, and the height was 22.45 ± 1.42 mm. For the core, the mean and standard deviation of the minor axis were 8.27 ± 0.33 mm, the major axis was 9.31 ± 0.42 mm, and the height was 12.65 ± 0.55 mm. Using an electronic balance, the mass of the fruits was measured to be 10.96 ±1.69 g, and that of the core was 0.56 ± 0.05 g. The densities of the Cerasus humilis fruits and cores were 1.05 ± 0.016 g/cm^3 and 1.15 ± 0.16 g/cm^3, respectively. The results of the mechanical property tests of the peel, pulp, and core of the Cerasus humilis fruits are shown in Figure 7.

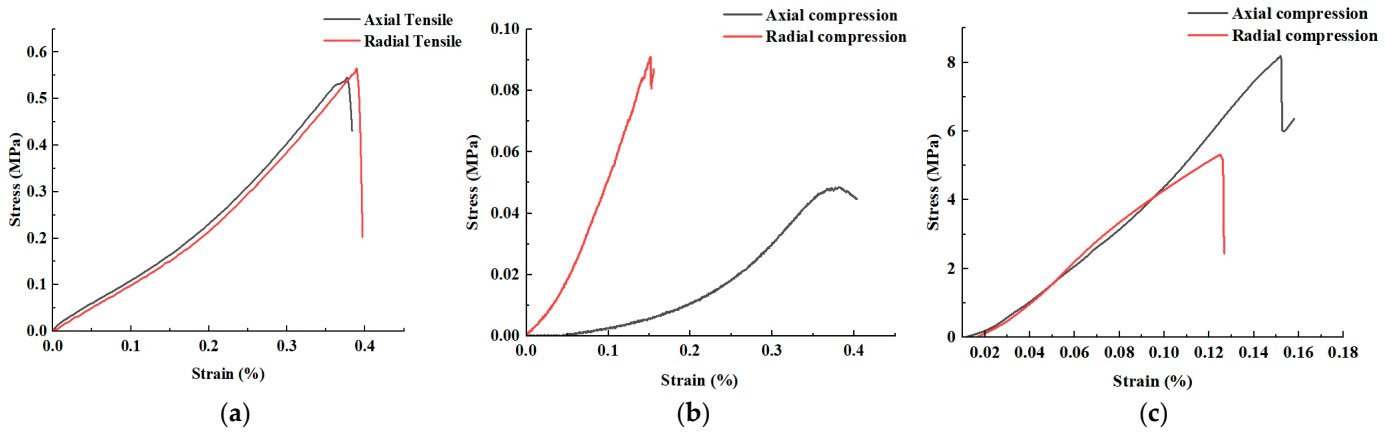

Figure 7. Mechanical property test results. (**a**) Axial and radial tensile stress–strain curves of peel; (**b**) axial and radial compressive stress–strain curves of pulp; (**c**) axial and radial compressive stress–strain curves of core.

From Figure 7a, it can be observed that when the peel of the Cerasus humilis fruits was stretched, both the axial and radial tensile stress–strain curves were nonlinear, with no

obvious bio-yield point. As the strain of the specimen increased, the stress correspondingly increased. When the strain reached a certain value, the stress reached its maximum. With a further increase in strain, the stress sharply decreased, and the peel fractured at this point. The point corresponding to the maximum stress is the failure point of the peel specimen; this stress is called the failure stress, which is the tensile strength of the peel [31]. The axial tensile strength of the peel was slightly greater than the radial tensile strength. From Figure 7b, it can be observed that the axial and radial compressive stress–strain curves of the pulp exhibited significant differences. During radial compression, the stress–strain curve showed a certain linear variation characteristic; as the load increased, the radial compressive stress gradually increased. When the stress reached the compressive strength of the pulp, its original tissue structure was destroyed, and the entire pulp fractured. In contrast, the axial compression curve displayed obvious nonlinearity, but the overall trend was similar to that in the radial direction. The radial compressive strength of the pulp was greater than the axial compressive strength, possibly because under axial compression, the pulp is more prone to sliding or deformation along the cell layers. From Figure 7c, it can be observed that the axial and radial compression curves of the core were similar to those of the peel. However, the axial compressive strength of the core was greater than its radial compressive strength. This may be because the fiber bundles or sclerenchyma cells inside the core are more densely arranged in the axial direction, thereby enhancing its axial load-bearing capacity.

The mechanical properties of the peel, pulp, and core of the Cerasus humilis fruits are presented in Table 3. A t-test of the experimental data indicated no significant differences between the axial and radial mechanical properties of the peel ($p > 0.05$), suggesting that the peel can be treated as an isotropic material. Conversely, significant differences were observed in the axial and radial mechanical properties of the pulp and core ($p < 0.05$), indicating that they exhibited anisotropic behavior. The detailed analysis results are provided in Table 4.

Table 3. Mechanical test results.

Material	Failure Load (N)		Compressive (Tensile) Strength (MPa)		Elastic Modulus (MPa)		Fracture Energy (mJ)	
	Axial	**Radial**	**Axial**	**Radial**	**Axial**	**Radial**	**Axial**	**Radial**
Peel	1.47	1.05	0.51	0.33	1.55	1.07	11.19	5.35
	1.23	1.39	0.54	0.35	1.24	1.18	12.33	8.88
	1.82	1.20	0.49	0.40	1.60	1.23	8.50	7.42
	1.81	0.95	0.45	0.38	1.09	1.42	11.6	5.16
	1.93	1.68	0.41	0.56	1.52	1.30	9.18	10.91
Average value	1.65	1.25	0.48	0.40	1.40	1.24	10.56	7.54
Standard deviation	0.29	0.29	0.05	0.09	0.22	0.13	1.64	2.43
Pulp	1.73	4.57	0.034	0.091	0.20	0.67	3.13	4.36
	2.65	3.82	0.053	0.076	0.28	0.52	4.51	3.34
	2.44	7.09	0.049	0.096	0.24	0.56	4.46	3.97
	2.51	4.66	0.05	0.087	0.23	0.51	4.98	5.40
	1.64	4.15	0.043	0.078	0.18	0.62	3.14	3.86
Average value	2.19	4.86	0.046	0.086	0.23	0.58	4.04	4.19
Standard deviation	0.47	1.29	0.0075	0.0085	0.038	0.068	0.85	0.77
Core	454.46	467.81	7.67	5.16	67.76	63.65	321.82	178.79
	479.06	521.50	7.78	5.74	73.29	66.40	351.71	228.17
	507.28	515.25	8.18	5.40	68.51	52.52	386.18	247.73
	476.61	468.37	7.93	4.98	78.37	61.71	362.08	166.19
	541.66	512.15	8.72	5.32	77.61	56.64	407.37	238.09
Average value	491.81	497.02	8.06	5.32	73.11	60.18	365.83	211.79
Standard deviation	33.59	26.62	0.42	0.28	4.94	5.57	32.75	36.81

Table 4. *t*-test results.

Material	Source of Variation	Factor	*t* Statistic	DF	*p*	Significance
Peel	Loading Direction	Failure Load	2.16	8	0.063	
		Compressive Strength	1.63	6	0.15	
		Elastic Modulus	1.38	6	0.21	
		Fracture Energy	2.30	7	0.055	
Pulp		Failure Load	−4.33	5	0.0074	*
		Compressive Strength	−7.84	8	<0.0001	*
		Elastic Modulus	−10.01	6	<0.0001	*
		Fracture Energy	−0.28	8	0.79	
Core		Failure Load	−0.27	8	0.79	
		Compressive Strength	12.11	7	<0.0001	*
		Elastic Modulus	3.88	8	0.0048	*
		Fracture Energy	6.99	8	0.00012	*

* indicates a significant difference, while a blank space indicates no significant difference.

3.2. Mechanical Properties of Cerasus Humilis Fruit

The stress–strain curves of the compressed Cerasus humilis fruits are shown in Figure 8. From Figure 8, it can be observed that the fruits exhibited a nonlinear stress–strain relationship during compression, and the axial and radial curves displayed certain similarities. The stress–strain curve exhibited a distinct biological yield point. When the stress reached the rupture point, the fruits completely fractured, followed by a decrease in stress. As the strain further increased and the indenter compressed the core, the stress rose again. The axial compressive strength of the Cerasus humilis fruits was higher than the radial compressive strength. This may be because, when subjected to axial compression, the peel and core provide greater support and resistance, causing Cerasus humilis fruits to exhibit a higher compressive strength during axial compression.

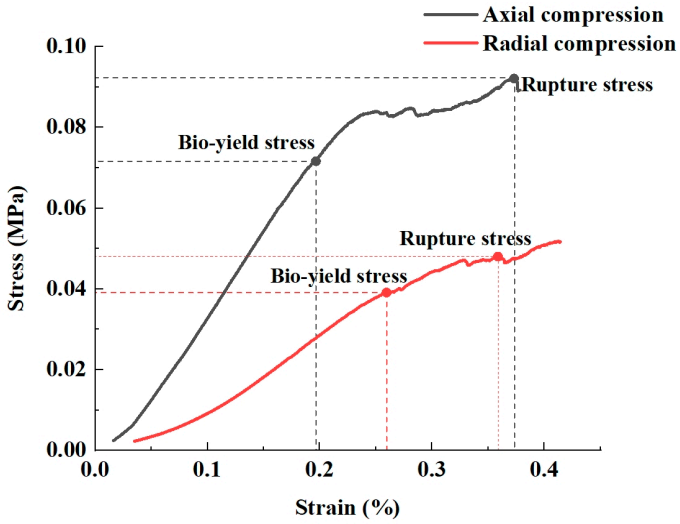

Figure 8. Stress–strain curves for axial and radial compression of Cerasus humilis fruits.

3.3. Finite Element Simulation Results and Analysis

To verify the accuracy of the finite element model, the force–displacement curves and damage conditions obtained from the simulation were compared and analyzed with those from the compression tests of the Cerasus humilis fruits, as shown in Figure 9. From Figure 9a,b, it can be observed that during the elastic stage, the experimental curves and simulation curves were highly consistent, indicating that the established finite element model can accurately represent the elastic characteristics of Cerasus humilis fruit. However, in the plastic stage, some deviations appeared between the simulation and experimental

curves: the force values obtained from the finite element simulation were slightly higher than the experimental results. This discrepancy may be attributed to the finite element model's limitations in fully accounting for the fruit's internal microstructure, such as intercellular voids and the distribution of tissue fluids, as well as the simplification of the material properties of the fruit's tissues into an elastoplastic model. We performed a fitting analysis between the simulation data and experimental data for the yielding stage of the fruit. The fitting results showed that the correlation coefficients between the simulation and experimental data were high (axial R^2 = 0.957, radial R^2 = 0.976). This indicates that the established finite element model can effectively be used to analyze the mechanical properties of Cerasus humilis fruit during the compression process. In terms of damage, Figure 9c shows the compression test results of a Cerasus humilis fruit, where a significant crack was observed along the central axis of the fruit during axial compression. Figure 9d presents the finite element simulation results, which reproduced a similar crack pattern and propagation trend. The crack positions and shapes in both cases were largely consistent, further demonstrating that the established finite element model can, to some extent, predict the deformation and fracture locations of these fruits, providing a reference for studying the fracture behavior of these fruits.

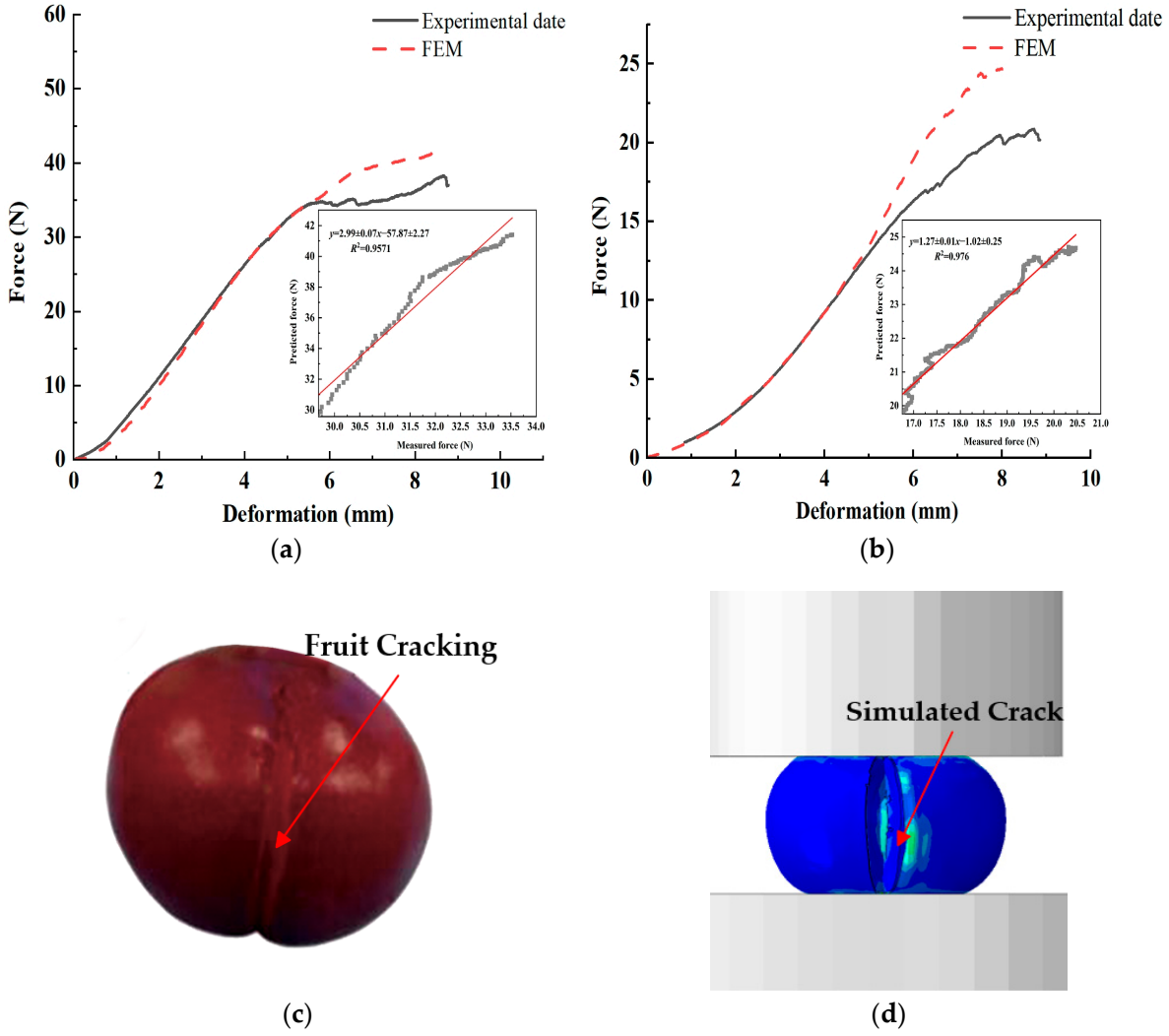

Figure 9. Comparison of simulation and experimental results. (**a**) Axial compression force–displacement curves; (**b**) radial compression force–displacement curves; (**c**) actual cracking; (**d**) simulated cracking.

At the onset of compression, the maximum stress was mainly concentrated in the regions where the Cerasus humilis fruit contacted the indenter and the support base. As the displacement of the indenter increased, the fruit gradually deformed. When the surface stress of the peel reached the critical damage value, the top and bottom of the fruit began to exhibit damage. As the displacement of the indenter further increased, the damaged areas gradually extended from the top and bottom toward the middle of the fruit. When the surface stress of the peel rose to 0.08 MPa, the peel completely ruptured, and the stress peak at the rupture location reached 0.75 MPa. After the peel ruptured, the pulp cells were damaged, and a large amount of tissue fluid exuded from the cracks. The damage process of the Cerasus humilis fruit is shown in Figure 10.

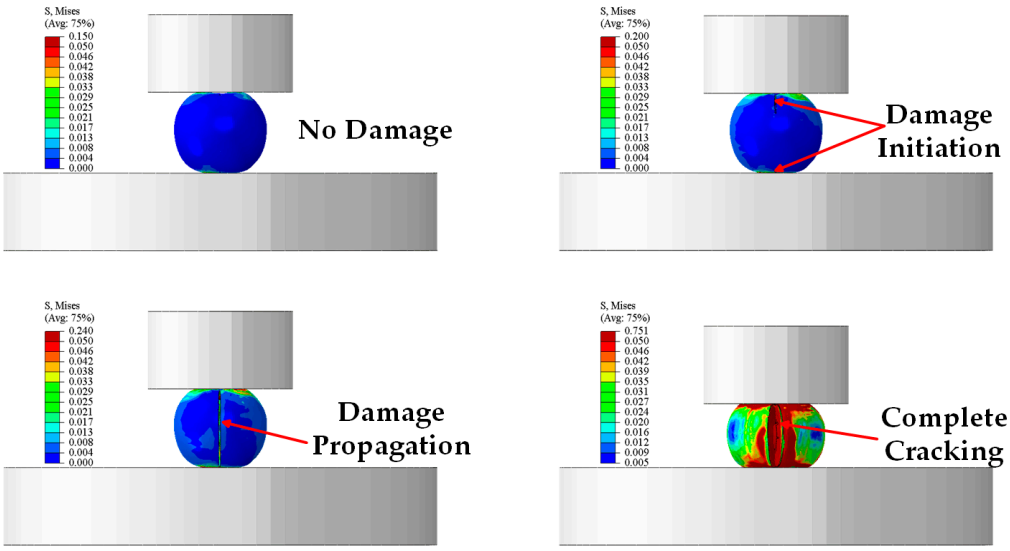

Figure 10. Cracking process of Cerasus humilis fruit.

3.4. Fruit Internal Damage Behavior

3.4.1. Internal Damage to Fruit Due to Axial Compression

In the Abaqus post-processing module, the Activate/Deactivate View Cut function was used to set the z-plane as the cutting plane, axially sectioning the Cerasus humilis fruit. The distribution of von Mises equivalent stress within the fruit at different compressive displacements is shown in Figure 11. During compression, the stress was transmitted from the peel to the core, exhibiting an axially symmetric distribution. When the compressive displacement was 1 mm, the maximum stress appeared at the contact points between the peel and the indenter and base, as well as at the bottom of the core. Since the maximum stress in the pulp region was lower than the axial yield strength of the pulp (0.05 MPa), no damage was observed in the fruit. When the compression displacement increased to 3 mm, the maximum stress occurred in the core region, and the stress in the pulp gradually propagated outward. In some areas, the stress exceeded the axial yield strength of the pulp, leading to the initiation of internal damage within the fruit. As the compression displacement reached 5 mm, the fruit entered the plastic deformation stage, and fine cracks began to appear on the surface of the peel. With further increases in compression displacement, these surface cracks gradually expanded toward the center. When the compression displacement reached 9 mm, the fruit underwent complete fracture.

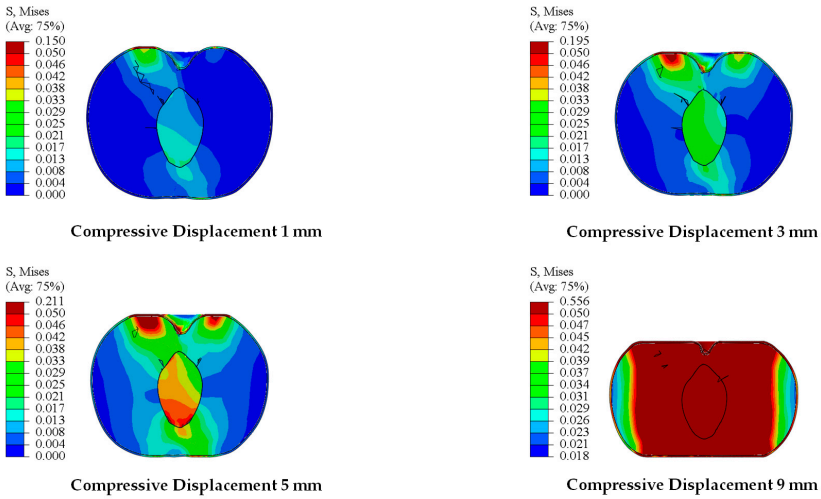

Figure 11. Axial von Mises stress distribution in Cerasus humilis fruit.

3.4.2. Internal Damage to Fruit Due to Radial Compression

Similarly, the distribution of von Mises equivalent stress within the fruit under different compressive displacements after radially sectioning the Cerasus humilis fruit is shown in Figure 12. The internal stress in the fruit exhibited a symmetrical distribution along its radial direction. When the compressive displacement was 1 mm, the maximum stress appeared at the contact points between the peel and the indenter and base; since the maximum stress in the pulp region was lower than the radial yield strength of the pulp (0.09 MPa), no damage was observed in the fruit. As the compression displacement increased, the stress in the pulp region gradually propagated toward the core. When the compression displacement reached 5 mm, internal damage began to develop within the fruit. At 6 mm, the fruit entered the plastic deformation stage, accompanied by the appearance of fine cracks on the peel's surface. With further increases in compression displacement, these surface cracks expanded toward the center, and the stress at the core reached its maximum. When the compression displacement reached 9 mm, the fruit underwent complete fracture.

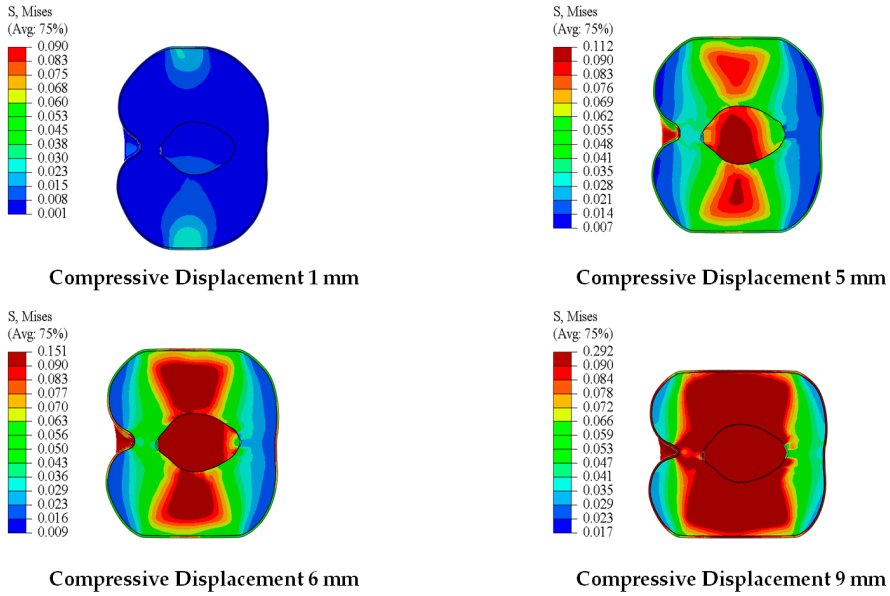

Figure 12. Radial von Mises stress distribution of Cerasus humilis fruit.

3.5. Discussion

Currently, the primary harvesting method for *Cerasus humilis* is comb-picking. During the harvesting process, compression caused by the comb teeth can lead to fruit damage. This damage can be categorized into two main types: direct surface cracking of the fruit and internal damage that is not easily visible to the naked eye. These damages severely affect the subsequent processing and storage of the Cerasus humilis fruit. This study simulated the damage behavior of Cerasus humilis fruit under compressive loading. The results showed that when the fruit entered the plastic stage, although the peel did not crack, large-scale internal damage had already occurred. Additionally, internal damage occurred earlier in the flesh when the fruit was subjected to axial compression, which is consistent with the findings in the literature [32,33]. When the compression displacement reached 9 mm, the fruit completely cracked. These results provide a theoretical basis for optimizing Cerasus humilis harvesting equipment and suggest minimizing axial compression on the fruit during the harvesting process.

Finite element simulation has been widely applied to study the mechanical behavior of fruits. Zou et al. [34] used the Burgers viscoelastic model to construct a simulation model for spinach, and the results showed that this model could effectively reflect the creep characteristics of spinach. Ma Shuai et al. [35] employed the Maxwell model to describe the mechanical properties of grape flesh and verified the accuracy of the model. In this study, a damage model based on elastic–plastic characteristics was used to simulate the compression damage process of Cerasus humilis fruit. However, the model did not account for the fruit's microstructural features and rheological properties. Future work will incorporate the fruit's microstructural characteristics and rheological properties to further refine the finite element model and improve the accuracy of damage prediction.

4. Conclusions

(1) Through mechanical testing, the mechanical parameters of various tissues of Cerasus humilis fruits were obtained in both the axial and radial directions. The fruit of Cerasus humilis exhibits anisotropic mechanical properties, with its axial compressive strength being higher than radial compressive strength.

(2) The Ductile Damage model was used to simulate the axial compression and cracking process of Cerasus humilis fruits. The simulation results showed that the force–displacement curve aligned well with the experimental data, and the fruit-cracking process closely matched the experimental observations. When the axial compression displacement reached 9 mm and the surface stress of the peel reached 0.08 MPa, the fruit underwent complete fracture. This model proved effective for simulating the damage behavior of Cerasus humilis fruits under compressive loading.

(3) During the compression process, the internal stress distribution of Cerasus humilis fruits was symmetrical, and the pulp tissue was more prone to damage. Under axial compression, internal damage began to appear when the displacement exceeded 3 mm, whereas in radial compression, internal damage started to occur when the displacement exceeded 5 mm.

Author Contributions: Conceptualization, C.H.; methodology, C.H. and D.Y.; software, C.H., D.Y., L.Z., J.Y. and T.W.; formal analysis, C.H. and T.W.; data curation, C.H., D.Y., L.Z., J.Y. and T.W.; writing—original draft, C.H.; writing—review and editing, C.H. and J.H. All authors have read and agreed to the published version of the manuscript.

Funding: This study was funded by the Shanxi Province Basic Research Program Project "Anti-Impact Evaluation Model for Mechanically Harvested Cerasus humilis Fruit and Exploration of New Harvesting Structures" (Project Number: 202203021221174).

Institutional Review Board Statement: Not applicable.

Data Availability Statement: Data are contained within the article.

Conflicts of Interest: The authors declare no conflicts of interest.

References

1. Zhang, X.; Guo, C.; Mu, X.; Guo, X.; Wang, P.; Wang, Z.; Cao, Q.; Du, J. Identification and expression analysis of ap2 gene family in chinese dwarf cherry [*Cerasus humilis* (bge.) sok]. *Mol. Plant Breed.* **2022**, *20*, 2162–2169. [CrossRef]
2. Wu, C.; Han, X.; Wu, J.; Wang, W.; Xie, C.; Xiao, B.; Zhou, Z.; Dong, X. Research progress on nutritional value and development and utilization of *Cerasus humilis* (bge.)sok. *China Fruits* **2024**, 1–5+25. [CrossRef]
3. Zhang, L.; Zhang, W.; Guo, J. Analysis of changes and correlations between calciums and organic acids in fruits of *Cerasus humilis* during different development stages. *J. Fruit Sci.* **2024**, *41*, 494–504. [CrossRef]
4. Kang, S.; He, J.; Wang, T. Study on single-branch combing of *Cerasus humilis*. *INMATEH Agric. Eng.* **2024**, *72*, 679–688. [CrossRef]
5. Liu, S.; He, J.; Wu, N. Design and experimental study of the comb-type harvesting test bench for *Cerasus humilis*. *INMATEH-Agric. Eng.* **2021**, *63*, 261–270. [CrossRef]
6. Du, X.; He, J.; He, Y.; Fang, D. Parameter optimisation and experiment on the combing of *Cerasus humilis*. *INMATEH-Agric. Eng.* **2019**, *57*. [CrossRef]
7. Hou, J.; Ren, Z.; Zhang, L.; Sun, Q.; Wang, W. Research on comb brush harvester and damage mechanism to material. A review. *INMATEH-Agric. Eng.* **2023**, *69*, 74–87. [CrossRef]
8. Yang, Y.; Yu, S.; Li, X.; Zang, H.; Xiao, A.; Liu, Y.; Su, G. Study on the effect of different harvest periods on the static pressure damage of korla fragrant pear. *Packag. Food Mach.* **2021**, *39*, 6–11. [CrossRef]
9. Tong, B.; He, J.; Zhou, J.; Wang, T.; Yang, H. Mechanical properties of *Cerasus humilis* at different temperatures for postharvest damage analysis. *INMATEH-Agric. Eng.* **2024**, *73*, 239–248. [CrossRef]
10. Xue, Z.; Zhang, X.; Chen, R. Experimental study on morphology and mechanical properties of pineapple. *J. Agric. Mech. Res.* **2024**, *46*, 170–174. [CrossRef]
11. Ihueze, C.C.; Mgbemena, C.E. Design for limit stresses of orange fruits (*Citrus sinensis*) under axial and radial compression as related to transportation and storage design. *J. Saudi Soc. Agric. Sci.* **2017**, *16*, 72–81. [CrossRef]
12. Zulkifli, N.; Hashim, N.; Harith, H.H.; Shukery, M.F.M. Finite element modelling for fruit stress analysis—A review. *Trends Food Sci. Technol.* **2020**, *97*, 29–37. [CrossRef]
13. Kang, S.; Lu, J.; Yang, H.; Guo, Y.; He, J. Mechanical model of *Cerasus humilis* established by uniaxial compression physical test and virtual simulation. *INMATEH-Agric. Eng.* **2023**, *69*, 527–536. [CrossRef]
14. Ihueze, C.C.; Okafor, C.E.; Onwurah, U.O.; Obuka, S.N.; Kingsley-omoyibo, Q.A. Modelling creep responses of plantain fibre reinforced HDPE (PFRHDPE) for elevated temperature applications. *Adv. Ind. Eng. Polym. Res.* **2023**, *6*, 49–61. [CrossRef]
15. Caglayan, N.; Oral, O.; Celik, H.K.; Cinar, R.; Rodrigues, L.C.D.A.; Rennie, A.E.; Akinci, I. Determination of time dependent stress distribution on a potato tuber during drop case. *J. Food Process Eng.* **2018**, *41*, e12869. [CrossRef]
16. Ben, Z.; Jibril, A.N.; Sun, X.; Bai, Y.; Yang, D.; Chen, K.; Dong, Y. Compression characteristics and fracture simulation of gluten pellet. *Foods* **2023**, *12*, 1598. [CrossRef]
17. *GB 5009.3-2016*; National Food Safety Standard-Determination of Moisture in Food. National Health Commission: Beijing, China, 2016.
18. Xie, Z.; Lang, Y.; Chen, L. A review of research on biomechanical properties of spheroid fruits. *J. Chin. Agric. Mech.* **2021**, *42*, 96–106. [CrossRef]
19. Wang, R.; Jiao, Q.; Wei, D. Determination of macromechanic parameters of grapes and tomatoes. *Trans. Chin. Soc. Agric. Eng.* **2004**, *20*, 54–57.
20. Tian, K.; Shen, C.; Li, X.; Huang, J.; Chen, Q.; Zhang, B. Mechanical properties and compression damage simulation by finite element for kiwifruit. *Int. Agric. Eng. J* **2017**, *26*, 191–201.
21. Chen, Y.; Cai, W.; Zou, X.; Xiang, H.; Liu, T.; Xu, F. Mechanical properties test and finite element analysis for litchi. *Trans. CSAE* **2011**, *27*, 358–363. [CrossRef]
22. Zhu, Y.; Zhu, L.; Guo, W.; Han, Z.; Wang, R.; Zhang, W.; Yuan, Y.; Gao, J.; Liu, S. Multiscale static compressive damage characteristics of kiwifruit based on the finite element method. *Foods* **2024**, *13*, 785. [CrossRef] [PubMed]
23. Liu, W.; Liu, T.; Zeng, T.; Ma, R.; Cheng, Y.; Zheng, Y.; Qiu, J.; Qi, L. Prediction of internal mechanical damage in pineapple compression using finite element method based on Hooke's and Hertz's laws. *Sci. Hortic.* **2023**, *308*, 111592. [CrossRef]
24. Han, B.; Su, G.; Zeng, Y.; Yang, J.; Fan, X.; Zhang, Y.; Zhang, H.; Wang, J. Fdem investigation on the crack propagation characteristics of walnut shell under multi-contact loadings. *Front. Mater.* **2023**, *10*, 1293683. [CrossRef]
25. Lang, Y.; Xie, Z.; Chen, L. Finite element simulation of mechanical properties of *Rosa roxburghii* under compression loading. *J. Food Process Eng.* **2022**, *45*, e13939. [CrossRef]

26. Andrade, F.; Feucht, M.; Haufe, A.; Neukamm, F. An incremental stress state dependent damage model for ductile failure prediction. *Int. J. Fract.* **2016**, *200*, 127–150. [CrossRef]
27. Brünig, M.; Brenner, D.; Gerke, S. Stress state dependence of ductile damage and fracture behavior: Experiments and numerical simulations. *Eng. Fract. Mech.* **2015**, *141*, 152–169. [CrossRef]
28. Seyedabadi, E.; Khojastehpour, M.; Sadrnia, H. Predicting cantaloupe bruising using non-linear finite element method. *Int. J. Food Prop.* **2015**, *18*, 2015–2025. [CrossRef]
29. Wu, N.; He, J.; Liu, S.; He, Y. Simulation and experiment of air screen cleaning device for *Cerasus humilis* based on edem-fluent coupling. *Agric. Eng.* **2021**, *11*, 82–87.
30. Fabbro, I.M.D.; Gazzola, J.; D' Avilla, E.; Silva, G.K.e.; Biasi, Â.R.; Enes, A.M.; Rodrigues, S. Physical and mechanical properties of biological materials. *Rev. Ciênc. Agron.* **2020**, *51*, e20207780. [CrossRef]
31. Ma, Q.; Guo, G.; Ma, J.; Lei, L.; Liu, K.; Long, H.; Li, J. Determination of mechanical characteristic parameters and extrusion crushing characteristics test for lotus seed kernel. *Trans. Chin. Soc. Agric. Eng.* **2018**, *34*, 263–271. [CrossRef]
32. Ashtiani, S.-H.M.; Sadrnia, H.; Mohammadinezhad, H.; Aghkhani, M.H.; Khojastehpour, M.; Abbaspour-Fard, M.H. Fem-based simulation of the mechanical behavior of grapefruit under compressive loading. *Sci. Hortic.* **2019**, *245*, 39–46. [CrossRef]
33. Liu, X.; Cao, Z.; Yang, L.; Chen, H.; Zhang, Y. Research on damage properties of apples based on static compression combined with the finite element method. *Foods* **2022**, *11*, 1851. [CrossRef]
34. Zou, L.; Yuan, J.; Liu, X.; Li, J.; Niu, Z. Burgers viscoelastic model-based variable stiffness design of compliant clamping mechanism for leafy greens harvesting. *Biosyst. Eng.* **2021**, *208*, 1–15. [CrossRef]
35. Ma, S.; Xu, L.; Xing, J.; Yuan, Q.; Duan, Z.; Yu, C.; Cheng, C. Study on collision damage experiment of grape and finite element analysis. *J. China Agric. Univ.* **2018**, *23*, 7. [CrossRef]